Stochastic Dynamic Analysis of Polar Sea Ice Variability

P. LEMKE, E. W. TRINKL AND K. HASSELMANN

Max-Planck-Institut für Meteorologie, Hamburg, Germany

(Manuscript received 29 February 1980, in final form 28 August 1980)

ABSTRACT

The analysis of Arctic (1966–76) and Antarctic (1973–79) sea ice data is presented, and a dynamical model based on white noise atmospheric forcing, local stabilizing relaxation and lateral diffusion and advection is constructed to explain the observations. Longitudinal dependent forcing, feedback, lateral diffusion and advection parameters are derived by fitting the model to the observed cross-spectral matrix of the sea ice anomaly fields. It is inferred that diffusion and advection of sea ice anomalies play an important role in sea ice dynamics. The model advection patterns agree reasonably well with the observed ocean surface circulation in the Arctic Ocean and around Antarctica.

1. Introduction

Interannual variations of the extent of sea ice are generally of the order of ⅓ of the seasonal excursion, and in individual years can be considerably larger. The ocean-atmosphere heat transfer changes significantly from ice-free to ice-covered regions of the ocean, and the anomalies may therefore be expected to appreciably affect the structure of the atmospheric circulation. In view of the long relaxation times of the anomalies, they are thus of considerable interest for the problem of extended range weather prediction and climate variability. Through the advent of satellites, data are now becoming available for larger-scale studies relevant to the question of ocean-ice-atmosphere interaction on the global scale. As a first step, we investigate the space-time structure of the sea ice anomaly fields of the Northern Hemisphere for the period January 1966–December 1976 and for the Southern Hemisphere for the period January 1973–February 1979. In concentrating on the statistical properties of the anomalies, our investigation may be regarded as complementary to other recent work on sea ice data (Sanderson, 1975; Walsh and Johnson, 1979a,b; Rayner and Howarth, 1979).

To describe the statistical properties of the anomaly fields we shall employ traditional representations in terms of empirical orthogonal functions, space and time lagged covariance functions and variance spectra. Although these representations are largely equivalent, each has certain advantages in emphasizing particular properties of the anomaly field. The interaction between sea ice anomalies and the atmospheric circulation is considered first in the simplest form in which the sea ice variability is modeled as the local response to a statistical independent, white-noise atmospheric forcing field. A similar model has been shown to provide a reasonable first-order description of sea-surface temperature variability in the interior of the ocean, away from strong current systems (Frankignoul and Hasselmann, 1977; Reynolds, 1978). The model also yields a reasonable first approximation of the observed sea ice variance spectra, and the concept of a dominantly one-way atmosphere-ice forcing mechanism is further supported by the asymmetrical structure of the atmosphere-ice correlation functions.

However, inspection of the cross-correlation functions of sea ice at different longitudes and the empirical orthogonal functions suggests that the interaction of ice anomalies in different areas plays an important role in sea ice dynamics, especially in the Southern Ocean. To account for this lateral interaction an extended model including lateral diffusion and advection, in addition to local feedback, is introduced. (Diffusion and advection represent, mathematically, the symmetrical and antisymmetrical components of a linear coupling with the neighboring longitudes.) It is found that with suitable choice of the longitudinal dependent forcing, feedback, diffusion and advection parameters most of the structure of the cross-spectral matrix of sea ice anomalies in the different regions of the ice covered ocean can be explained. It is inferred that both lateral diffusion and lateral advection play an important role in sea ice dynamics, especially in the Southern Ocean, where the ice-ocean coupling appears to be more pronounced, presumably through upwelling and strong ocean currents. The inferred advection pattern of sea ice anomalies is in reasonable agree-

0022-3670/80/122100-21$09.25

ment with the observed ocean surface circulation at both polar regions.

In contrast, to deterministic models which are usually designed to simulate the seasonal cycle of sea ice cover, thickness and drift as the response to observed seasonal varying forcing fields [winds, air temperature, solar radiation (see Hibler, 1979; Parkinson and Washington, 1979)], our statistical models are applied in the inverse modeling sense to determine certain time independent dynamical parameters (local feedback, diffusion, advection and white noise atmospheric forcing) as optimal least squares fits to the observed variations of sea ice anomalies in space and time. By applying a hierarchy of models, the degree of detail about the physics of the system that can be inferred from the existing limited data set can be systematically established.

A more detailed analysis of the ice-atmosphere feedback branch will be carried out in a separate investigation. The main purpose of the present analysis is to establish the magnitude and characteristic space and time scales of the sea ice anomaly field itself, and to estimate the characteristic dynamical parameters required to explain the observed anomalies as a guide for constructing more sophisticated dynamical models of the coupled ocean-ice-atmosphere system based on more detailed physics.

2. The data base

Our eleven-year Arctic data record (January 1966–December 1976) is based on the monthly Northern Hemisphere sea ice charts published by the United Kingdom Meteorological Office (MO), Bracknell. The data were digitized in 10° longitudinal sectors by counting the number of 1° rectangles of sea ice within each 1° band of latitude within a given 10° longitudinal sector. The ocean was regarded as ice-covered if the MO chart indicated at least 70% ice cover. Open pack ice, also indicated on the maps, was not included. This data was then used to determine the total sea ice area within a 10° longitudinal sector, as well as additional geometric variables, such as the center of mass of the ice-covered area within each sector. These were not used, however, in the following analysis.

Until December 1972 the MO charts contain areas with uncertain ice boundaries due to the lack of reliable data. These regions generally occur mainly in the winter north of the coasts of the USSR, Alaska and Canada. For most of the questionable areas and periods it can be assumed, however, that the ice limit extends to the northern coastline bounding the Arctic Ocean, so that the lack of data should have no serious impact on the anomaly analysis. The two regions which are perhaps most strongly affected by data gaps are the eastern Barents Sea and the Bering Sea. The Bering Sea region suffers from the additional handicap that its southern part is not covered by the MO charts, so that our analysis includes only data north of 65°N in this region. Despite these shortcomings, the Arctic data was considered sufficiently complete in time and space to carry out a meaningful statistical analysis of the larger scale properties of the anomaly fields.

The 6-year Antarctic data set (4 January 1973–22 February 1979) is based on the weekly Southern Hemisphere sea ice charts published by the U.S. Fleet Weather Facility (FLEWEAFAC), Suitland, Maryland. The charts were digitized by reading the latitude of the ice edge (concentration larger than 5/8) on a 5° longitudinal grid, but a 10° longitudinal grid was then used for the actual analysis.

3. The annual cycle

An annual cycle was determined in the standard manner by averaging the sea ice area (ice margin, in the case of Antarctica) values for each month (week) at each longitude interval over the eleven years (five years) of data. The results of this section may be compared with similar analysis carried out by Sanderson (1975), Walsh and Johnson (1979a), Gordon and Taylor (1975), Rayner and Howarth (1979) and Ackley (1979a). The seasonal cycle of Arctic sea ice cover for 10° longitudinal sectors centered at selected longitudes is shown in Fig. 1. Fig. 2, (solid line) shows the longitudinal distribution of the root mean square variation of the annual sea ice cycle for the Arctic. The radial coordinate of the curve is proportional to the square root of the rms ice area, so that the area between the Pole and the curve in a given sector is in fact proportional to the rms ice extent within that sector. (However, the curve cannot be identified with the sea ice boundary itself, since the land areas were subtracted from the total ice areas, and the areas shown represent the seasonal variations of the ice area relative to the mean ice cover.)

The figures clearly illustrate the pronounced regional variability of sea ice. As is well-known, the strongest annual changes are observed in the regions west and east of Greenland, the Barents Sea, the eastern Laptev Sea and the Bering Sea, the smallest in the Beaufort Sea and the West Canadian sectors. The regional variability may be largely attributed to the geometry of the coastal boundaries, which intersect the annually extending and contracting ice cap at different latitudes and angles, thereby affecting the area of the ocean exposed to sea ice formation in the different sectors and the direction of growth of the sea ice boundary. However, exposure of the ocean areas to continental or maritime climatic conditions also contributes to regional variability through variations in the seasonal amplitudes of the heating and cooling rates.

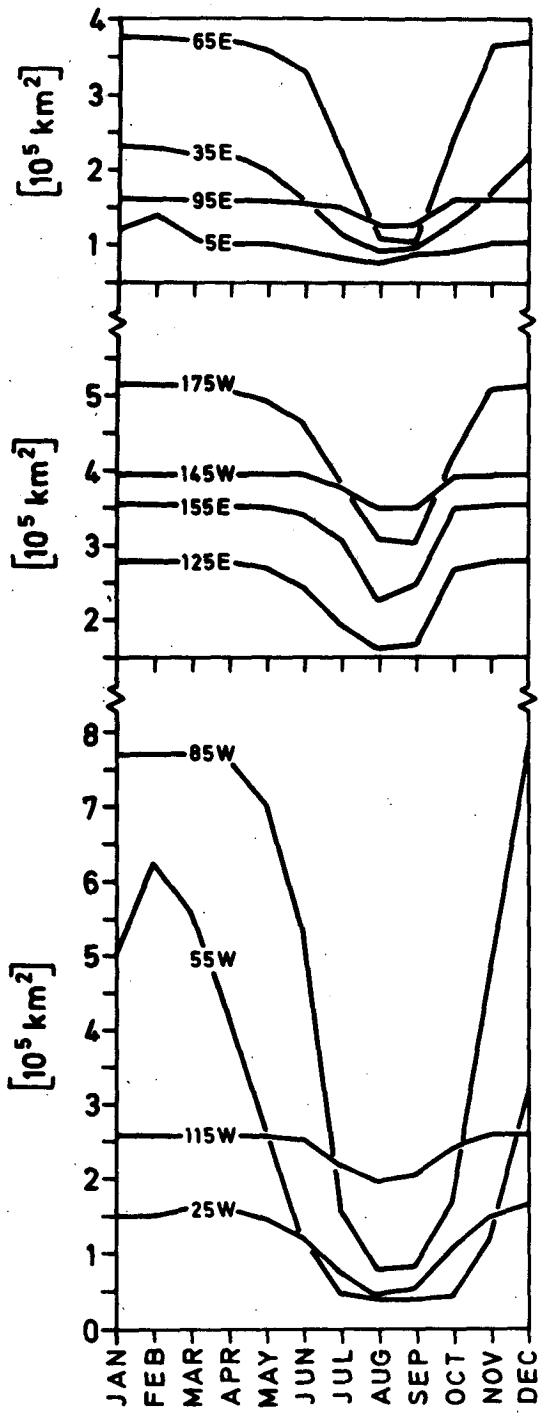

FIG. 1. Seasonal cycle of Arctic sea ice cover in 10° longitudinal sectors centered at various longitudes.

The annual cycle of the ice edge at different longitudes in the Southern Ocean is shown in Fig. 3. Minimum and maximum sea ice extent occurs in different regions at slightly different times of the year. The annual cycle of the total ice cover shown in Fig. 4 is more pronounced in the Southern Ocean than in the land locked Arctic Basin. The Arctic and Antarctic sea ice cycles also differ in their growth-melt asymmetry. Sea ice in the Arctic Ocean exhibits faster seasonal creation than melting, whereas the opposite is true for the Southern Ocean. The asymmetric annual cycle in the Antarctic (fast melting, slow freezing) is consistent with observations by Rayner and Howarth (1979). Asymmetries of this type can be explained only by nonlinear processes, such as a dependence of the ice-ocean feedback on the variable depth of the mixed layer. However, this question was not pursued further, since the necessary observations for a quantitative model were not available.

The longitudinal dependence of the seasonal variation of the sea ice margin in the Southern Ocean is illustrated in Fig. 5. The strongest annual changes are found in the Weddell Sea and the Ross Sea. These two areas are known as the ice factories of Antarctica and also as the two major areas of Antarctic bottom water formation—a result of brine expulsion during the freezing process. The smallest annual changes are observed in the South Indian Basin, the Bellinghausen Sea and around the Antarctic Peninsula, where strong upwelling regions (Gordon *et al.*, 1977) and the Antarctic Circumpolar Current prevent northward flow of sea ice. The geographic relations are illustrated by Fig. 6, which shows the annual mean sea ice limit and the corresponding distributions for the minimum ice cover in late February and the maximum ice cover in early October.

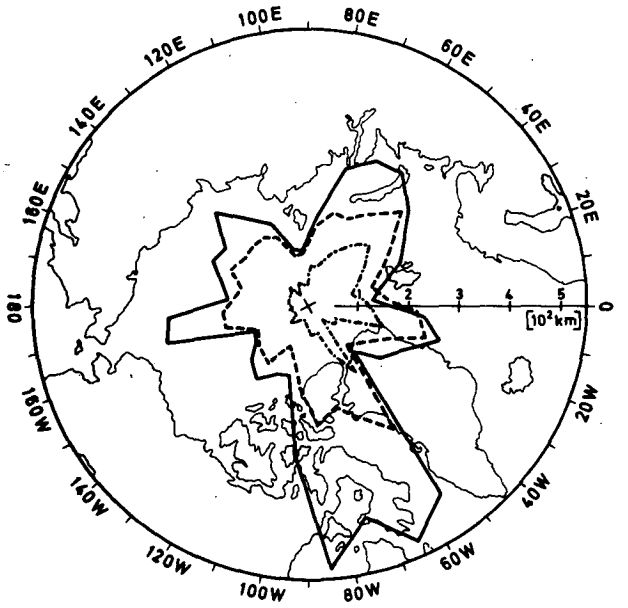

FIG. 2. Longitudinal distribution of the root mean square variability of the annual Arctic sea ice variation (solid line), the anomaly field (dashed line) and the square root of the variance corresponding to the linear trend (dash-dotted line).

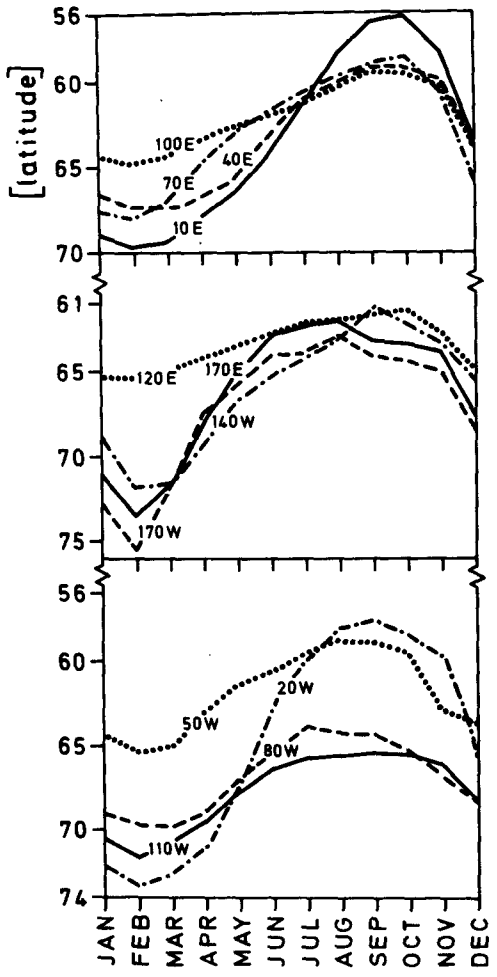

FIG. 3. Seasonal cycle of the Antarctic sea ice margin at various longitudes.

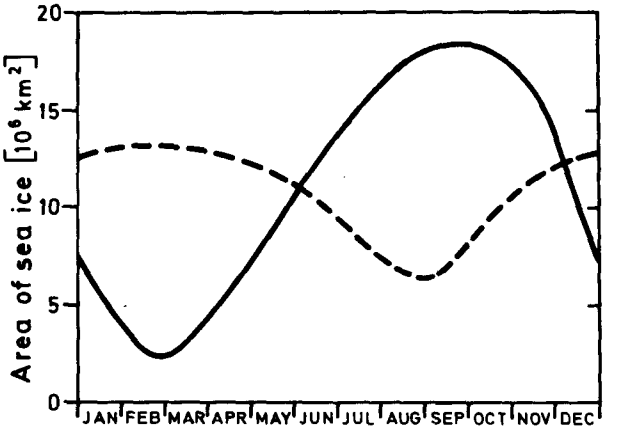

FIG. 4. Annual cycle of the total Arctic (dashed line) and Antarctic (solid line) sea ice cover.

4. The anomaly field

a. Trend

Figs. 2 and 5 show, in addition to the annual cycles, the longitudinal distribution of the rms sea ice anomaly field, defined in the usual manner as the residual sea ice area after subtraction of the annual cycle (dashed line). The anomaly variance of the sea ice area exhibits approximately the same longitudinal dependence as the annual cycle in both hemispheres, but is only about ⅓ as large (in terms of rms area).

We shall be concerned primarily with fluctuations of the anomaly fields at periods shorter than about two years which can still be treated statistically with the available lengths of data series. For this purpose it is sometimes advisable to detrend the data, although this was found to have little influence in the present case and was therefore not done. However, the trend itself is also of interest as at least a single sample representative of the longer period anomaly fluctuations which cannot be adequately resolved in a statistical sense with the existing data.

The anomaly time histories of Arctic sea ice shown in Fig. 7 for three typical longitudes and for the total ice covered area indicate a positive trend at 55°W and a negative trend at 15°W, 15°E and for the total area. (The linear trend is denoted by a dashed line.) The mean retreat of the total Arctic sea ice cover from 1966 to 1976 is 4×10^4 km² per year and accounts for 17% of the total anomaly variance. Fig. 8 summarizes the longitudinal distribution of the linear trend (first order polynomial fitted to the time series)

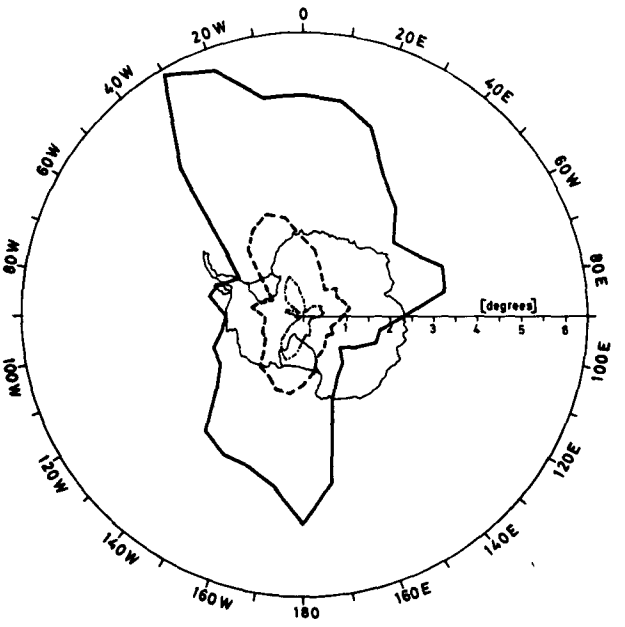

FIG. 5. Longitudinal distribution of the root mean square variability of the annual Antarctic sea ice variation (solid line), the anomaly field (dashed line) and the square root of the variance corresponding to the linear trend (dash-dotted line).

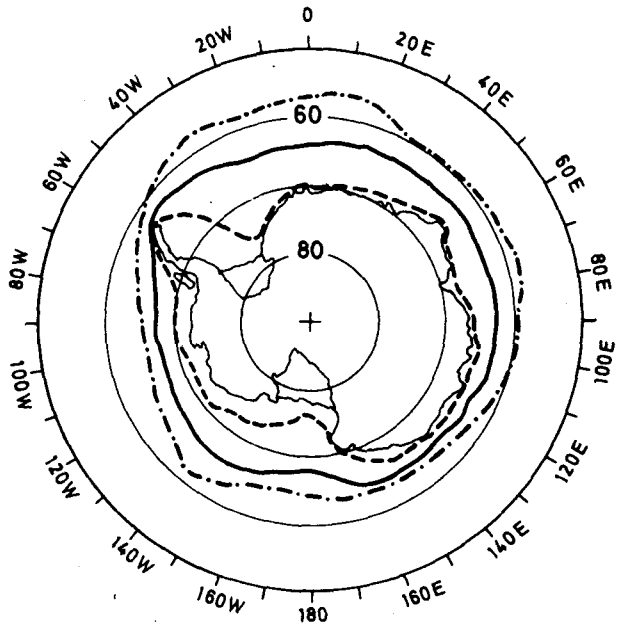

FIG. 6. Longitudinal distribution of the annually averaged sea ice limit (solid line), the minimum sea ice extent at the end of February (dashed line) and the maximum sea ice extent in early October (dash-dotted line). The curves apply for the average annual cycle from 1973–79.

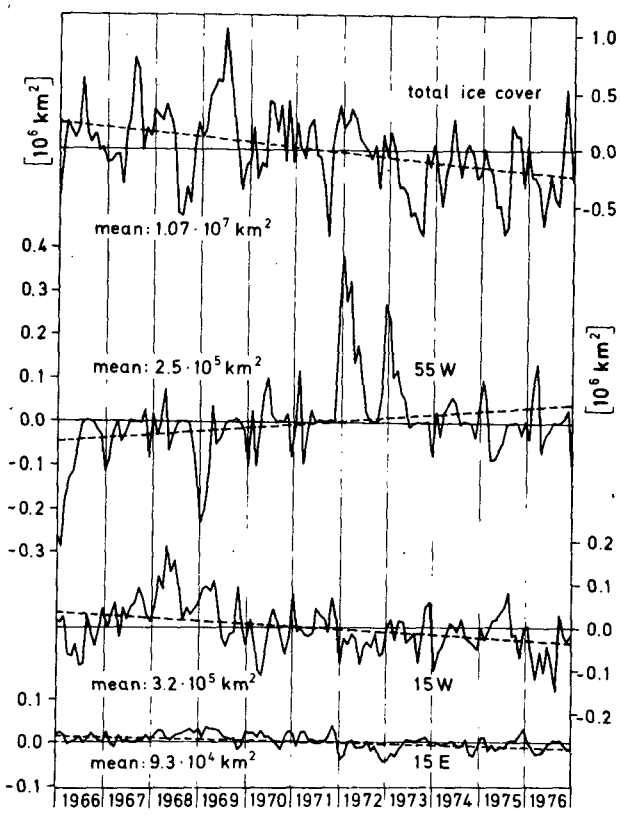

FIG. 7. Anomaly time histories (solid lines) and linear trend (dashed lines) of the total ice covered area in the Arctic and the sea ice cover in 10° longitudinal sectors centered at various longitudes.

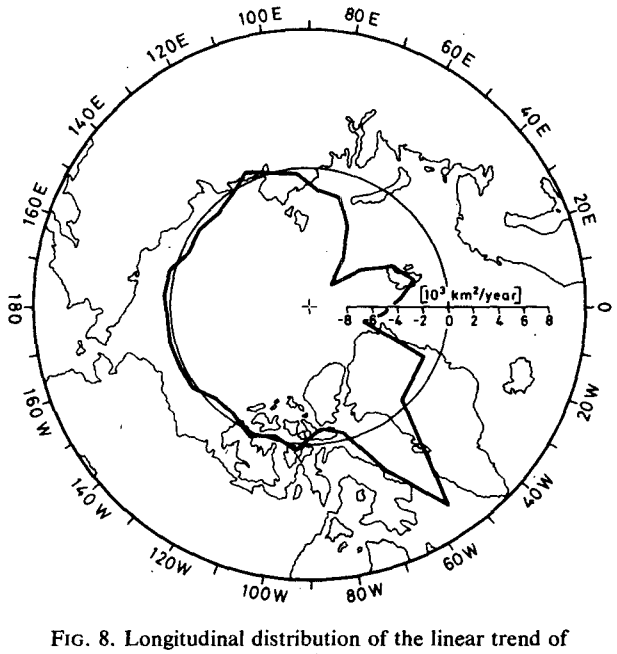

FIG. 8. Longitudinal distribution of the linear trend of Arctic sea ice cover.

of the sea ice cover in the Arctic for all sectors. There is a large negative trend in the eastern Atlantic region and a large positive trend in the Davis Strait sectors. This may be attributed to the well-known seesaw relation between West Greenland and Norwegian air temperatures (van Loon and Rogers, 1978), which is also seen later in the cross-correlation of the sea ice anomalies and in their first empirical orthogonal function (Fig. 12). The trend in the land locked Siberian and Canadian sectors is much smaller than in the sectors open to the Atlantic. This is consistent with observations by Sanderson (1975) who also found a positive trend in the East Canadian sector and a negative trend in the Greenland and Barents Sea sectors. The mean retreat of the total Arctic sea ice cover in the five months investigated (February, March, April, August, September) from 1969 to 1974 was found to be 1% per year, compared to our result of 0.4% per year for the complete 11 year period 1966–76. The anomaly time histories of the Antarctic sea ice edge at three typical longitudes and for the total sea ice covered area (Fig. 9) show a negative trend denoted by the dashed lines. The retreat of the total Antarctic sea ice cover from January 1973 to February 1979 is 4×10^5 km^2 per year, and accounts for 40% of the total anomaly variance. Inspection of the longitudinal distribution of the linear trend (Fig. 10) indicates that the sea ice is retreating in most parts of the Southern Ocean. The only positive trend is observed in the Bellinghausen Sea (80°W). An anti-phase relation between the Bellinghausen Sea and the Weddell Sea is also found in the cross-correlation of the sea ice anomalies and in the first empirical orthogonal function

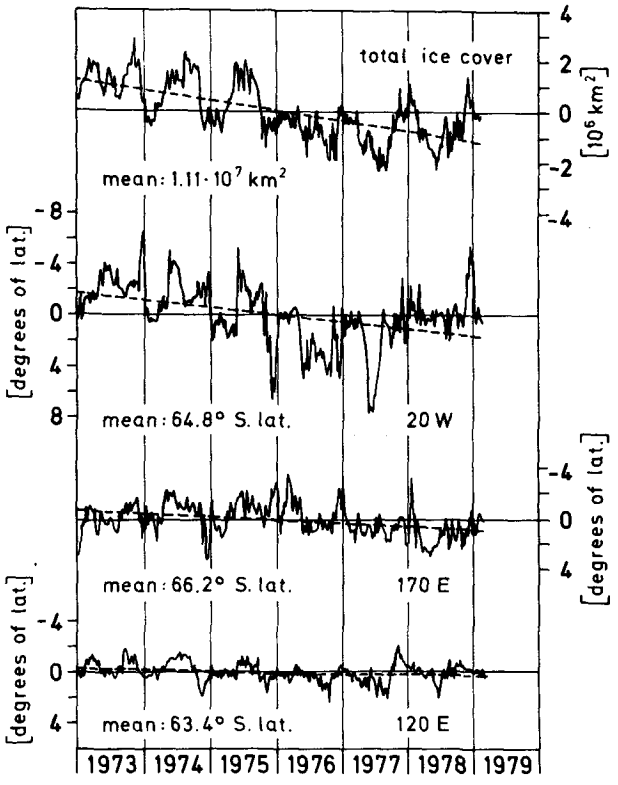

FIG. 9. Anomaly time histories (solid lines) and linear trend (dashed lines) of the total Antarctic sea ice cover and the sea ice edge at various longitudes.

(Fig. 13). The longitudinal distribution of the variance associated with the linear trend is shown as a dashed-dotted line in Figs. 2 and 5.

b. Spatial and time structure

1) EOF REPRESENTATION

The examples of the anomaly time histories of individual sectors and of the total sea ice area for the Arctic shown in Fig. 7 and Antarctic in Fig. 9 suggest some degree of correlation between the anomalies in different regions. A useful statistical description of the spatial correlation structure of the anomaly field is the decomposition into empirical orthogonal functions (EOF's) or principal components (cf. Lorenz, 1956).

Fig. 11 shows the relative contributions to the total variance of the sea ice anomaly field from the various EOF components for the Arctic and Antarctic. The strong downward curvature of the cumulative variance curves indicates the success of the EOF representation in ordering the more important spatial patterns. Over 80% of the total variance is contained in the first eight EOF's for both hemispheres. The EOF patterns themselves are shown, together with the square root of the total variance curve σ for comparison, in Figs. 12 and 13. With the

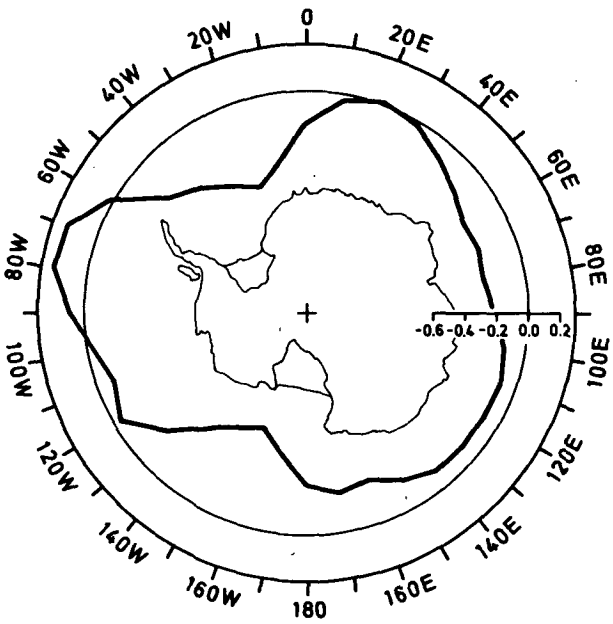

FIG. 10. Longitudinal distribution of the linear trend of Antarctic sea ice cover in degrees of latitude per year.

exception of the Bering Sea area, the first four EOFs for the Arctic agree very well with the EOF's determined by Walsh and Johnson (1979b) from 25 years of data (allowing for the difference in the arbitrary sign of the EOF's 2 and 3). The disagreement in the Bering Sea is probably due to the fact that our analysis includes only sea ice north of 65°N in this area (due to the limitation of the British sea ice chart formats), and Walsh and Johnson introduced additional sea ice information in this region. The lower-order EOF's are seen to be associated generally with larger spatial scales. For $m \geq 6$, the longitudinal structure of the EOF's has the appearance of white noise. The longitudinally-correlated components of the sea ice anomaly field (for lags greater than 10° longitude) can probably be adequately represented by only five EOF's. The dominant first EOF pattern for the Arctic contains strong lobes of opposite sign

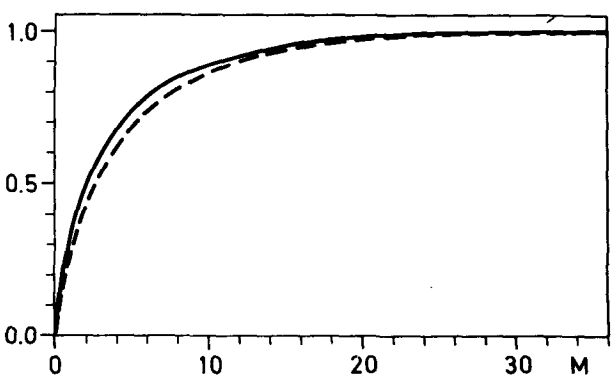

FIG. 11. Cumulative EOF variance of Arctic (dashed line) and Antarctic (solid line) sea ice.

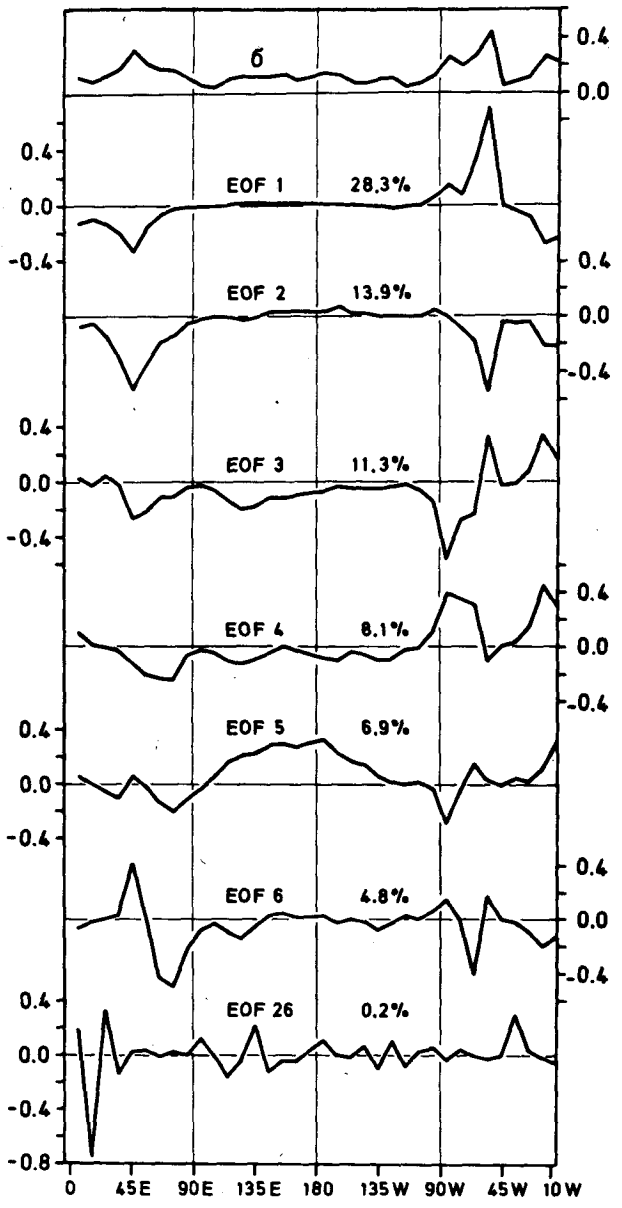

FIG. 12. Longitudinal distribution of the square root of the anomaly variance σ and EOF patterns of Arctic sea ice variability.

in the East Canadian and Barents Sea sectors, consistent with the negative correlation between these longitudes.

The main contribution to the first EOF of the Antarctic sea ice comes from the Weddell Sea, whereas the second EOF is mainly determined by the Ross Sea area, suggesting that the two principal "ice factories" in the Southern Ocean are nearly decoupled.

2) AUTOCORRELATION FUNCTION OF THE EOF AMPLITUDES

The EOF patterns provide a complete description of the second moment structure of the anomaly fields at different positions at the same time. A complete second moment description, however, should include also time-lagged correlations. These can be considered either in terms of the original anomaly fields $y_i(t)$ or in terms of the amplitudes $c_i(t)$ with respect to the EOF vector basis. Figs. 14 and 15 show the diagonal terms

$$S_i(\tau) = \frac{\langle c_i(t+\tau)c_i(t)\rangle}{\langle c_i(t)c_i(t)\rangle}$$

of the correlation matrix in the EOF representation. The nondiagonal terms contain relatively little information in the EOF representation; they vanish for $\tau = 0$ on account of the orthogonality of the EOF coefficients and remain small also for non-zero τ. A discussion of the complete time-lagged covariances matrix is given in terms of the physical sector representation in the following section. Figs. 14 and 15 show clearly that the correlation time scales decrease with increasing order of the EOF's, indicating that sea ice variations on larger spatial scales (lower EOF's, cf. Figs. 12, 13) are associated with large relaxation times. This scale dependence of

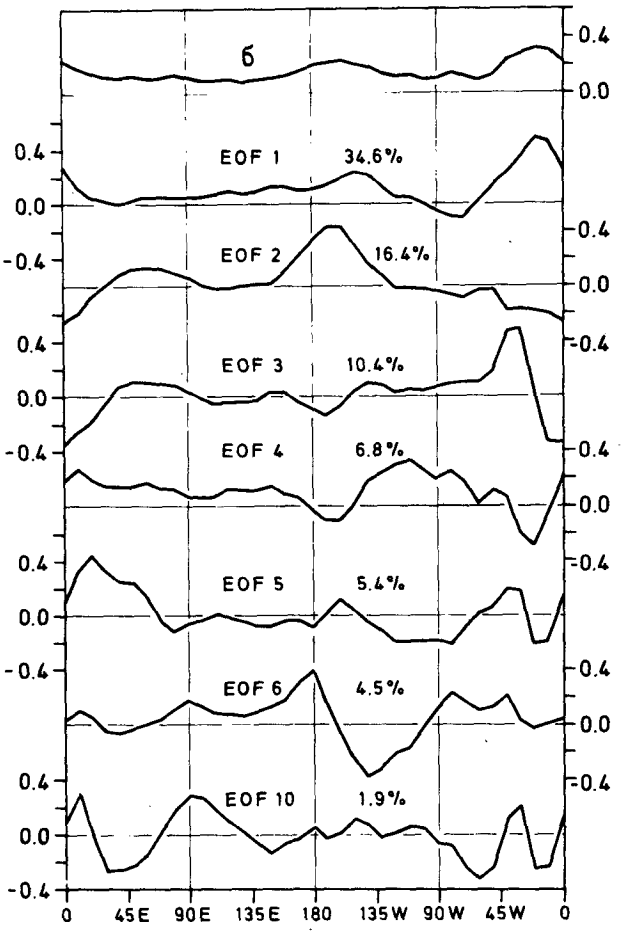

FIG. 13. Longitudinal distribution of the square root of the anomaly variance σ and EOF patterns of Antarctic sea ice variability.

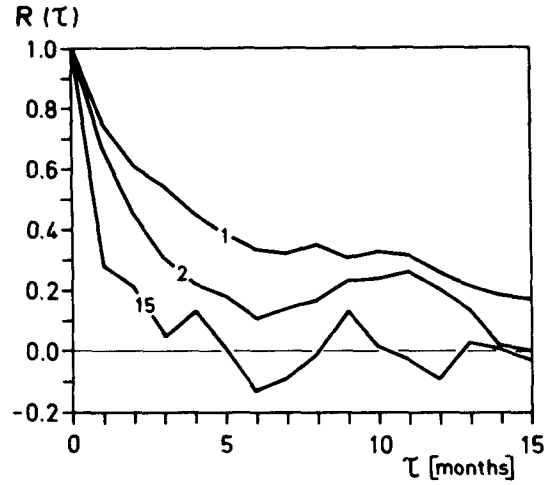

FIG. 14. Autocorrelation functions of the amplitudes of the first two and the fifteenth EOF of Arctic sea ice variability.

the relaxation time is discussed in more detail in Lemke (1980).

3) SECTOR REPRESENTATION

An alternative, and more complete description of the space-time structure of the second moment field is given in Figs. 16 and 17 in terms of the cross-correlation functions

$$R_{ij}(\tau) = \frac{1}{N-\tau} \sum_{t=1}^{N-\tau} y_i(t) y_j(t+\tau) \qquad (1)$$

as a function of the sector lag $i-j$ for different time lags τ and different reference sectors i. (N is the length of the time series.) Also shown is the zonally-averaged covariance function

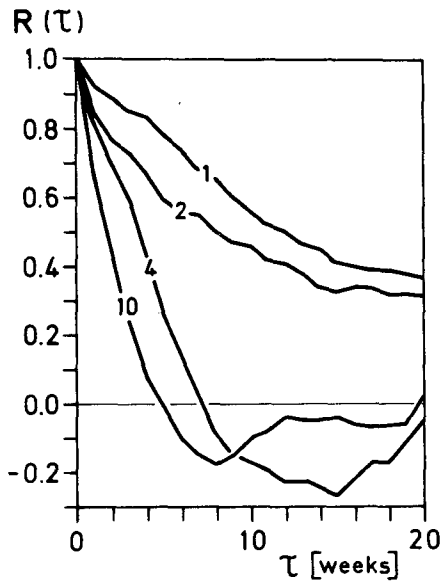

FIG. 15. Autocorrelation functions of the amplitudes of the first two, the fourth and the tenth EOF of Antarctic sea ice variability.

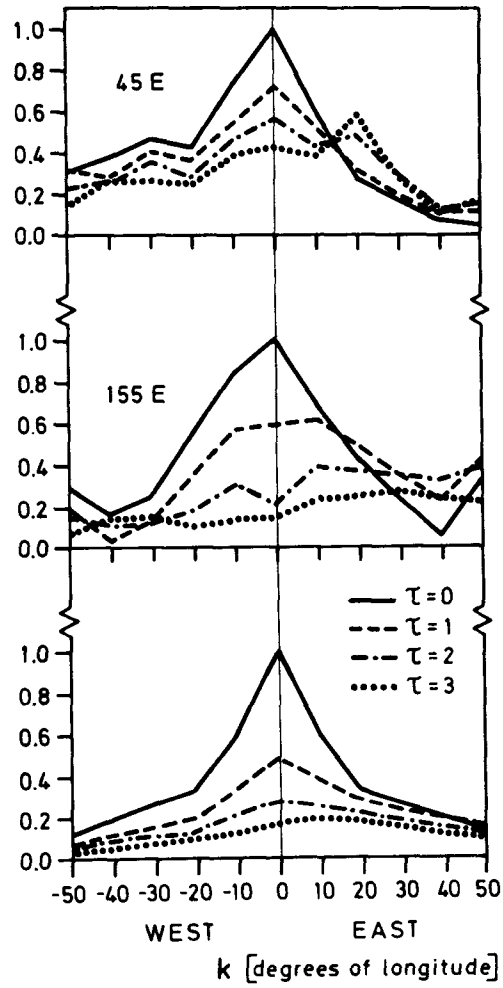

FIG. 16. Arctic cross-correlations $R_{i,i+k}(\tau)$ for different time lags, (τ = 0, 1, 2, 3 months) as functions of longitudinal lag k for longitudes i = 45°E and i = 155°E. Also shown is the zonally-averaged cross-correlation $\bar{R}_k(\tau)$.

$$\bar{R}_k(\tau) = \frac{1}{36} \sum_{i=1}^{36} R_{i,i+k}(\tau). \qquad (2)$$

The pronounced east-west asymmetry of the cross-correlation functions in Fig. 17 indicates that advection of ice anomalies plays an important role in large-scale sea ice dynamics in the Southern Ocean. Ice anomalies in the South Indian Basin (130°E) tend to propagate from west to east, whereas the propagation is from east to west in the Amundsen Sea (120°W). Inspection of other cross-correlations suggest an eastward drift of ice anomalies in most parts of East Antarctica and a westward drift in the Weddell Sea, the Ross Sea and the Amundsen Sea. This is in qualitative agreement with straightforward anomaly advection, or with feedback models postulating closed ice-ocean-ice or ice-atmosphere-ice feedback in the presence of prevailing winds or ocean currents (Antarctic Circumpolar Current,

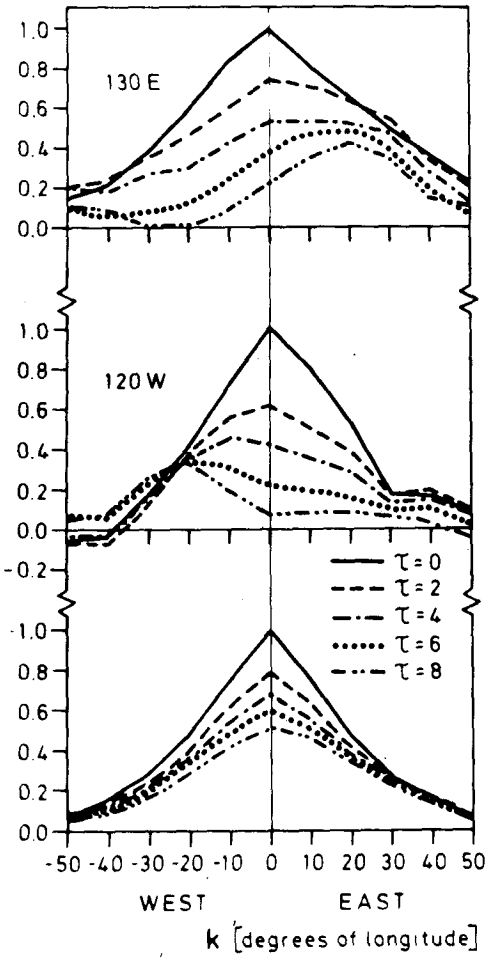

FIG. 17. Antarctic cross-correlations $R_{i,i+k}(\tau)$ for different time lags, (τ = 0, 2, 4, 6, 8 weeks) as a function of longitudinal lag k for longitudes i = 130°E and i = 120°W. Also shown is the zonally-averaged cross-correlation $\bar{R}_k(\tau)$.

gyres in the Weddell Sea, the Ross Sea and the Amundsen Sea. A surface current map is given in Fig. 31, after Treshnikov, 1967). In the Arctic Basin lateral propagation seems to be of minor importance. The cross-correlation functions (Fig. 16) exhibit only a weak eastward asymmetry. (The 95% confidence level of uncoupled Markov time series is smaller than 0.1 in both figures.) A general dynamical model fitted to the cross-spectral matrix of sea ice anomalies which reproduces the propagation effects apparent in Figs. 16 and 17 will be discussed in Section 7.

Examination of the entire cross-correlation function $R_{ij}(\tau)$ demonstrates that strong correlations between ice anomalies at different longitudes exist essentially only for longitude lags of 10–20°. In the Arctic strong correlations on a larger spatial scale are observed only in the Atlantic and Siberian sectors. In the Southern Ocean distant cross correlations are found in the Weddell Sea, the South Indian Basin and the Ross Sea. In general, the spatial scale of the Antarctic cross correlations is slightly larger than in the Arctic (Lemke, 1980).

Figs. 18 and 19 finally show examples of the variance auto-spectra of the sea ice anomalies for individual longitudes in the Arctic and Antarctic. Also shown are the best-fit autospectra (solid lines)

$$\hat{G}_i(\omega) = \frac{\hat{F}_i}{1 + \alpha_i^2 - 2\alpha_i \cos(\omega\Delta)}, \tag{3}$$

corresponding to a first-order discrete Markov-process (Jenkins and Watts, 1968)

$$y_i(t) = \alpha_i y_i(t - \Delta) + n_i(t), \tag{4}$$

where $\hat{F}_i$ represents the (constant) variance spectrum of the white noise forcing function $n_i(t)$.

The continuous differential form corresponding to the discrete form (4) is given by

$$\dot{y}_i(t) = -\lambda_i y_i(t) + \hat{n}_i(t), \tag{5}$$

where

$$\lambda = \frac{1 - \alpha}{\Delta} \quad \text{and} \quad \int_{t-\Delta/2}^{t+\Delta/2} \hat{n}dt = n \tag{6}$$

and $\lambda > 0$ ($|\alpha| < 1$) for a stable Markov process.

The feedback parameter λ and the level of the white noise forcing $\hat{F}$ were determined by a least-

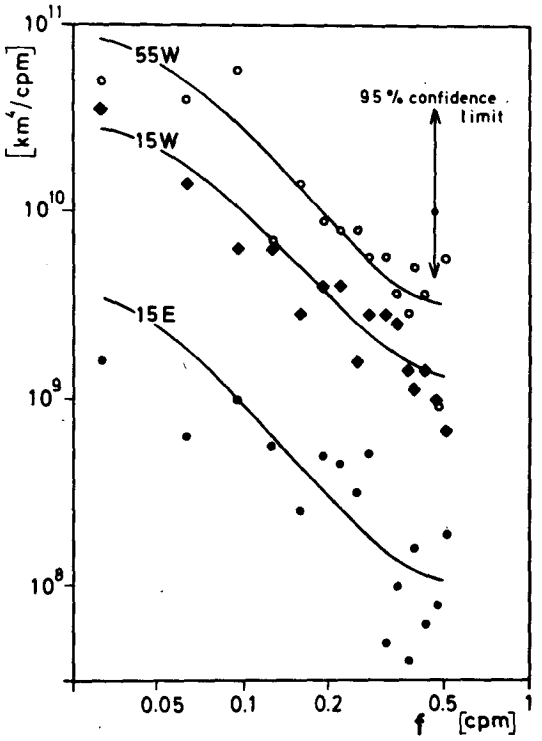

FIG. 18. Variance auto-spectra of Arctic sea ice anomalies at three typical longitudes and fitted first-order Markov models (solid lines).

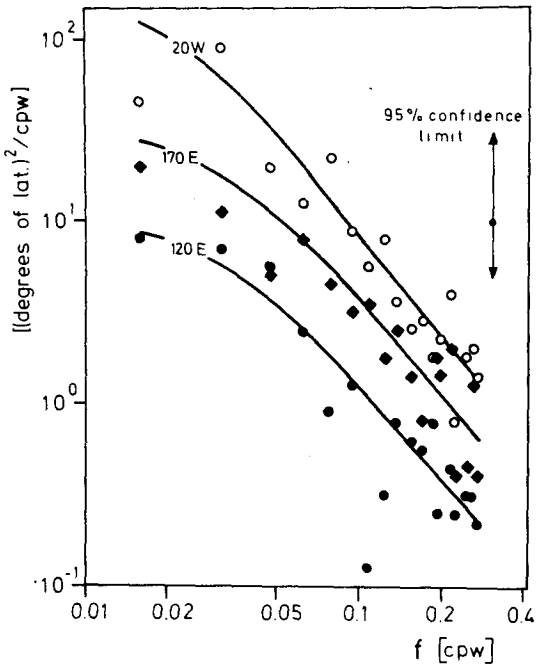

FIG. 19. Variance auto-spectra of Antarctic sea ice anomalies at three typical longitudes and fitted first-order Markov models (solid lines).

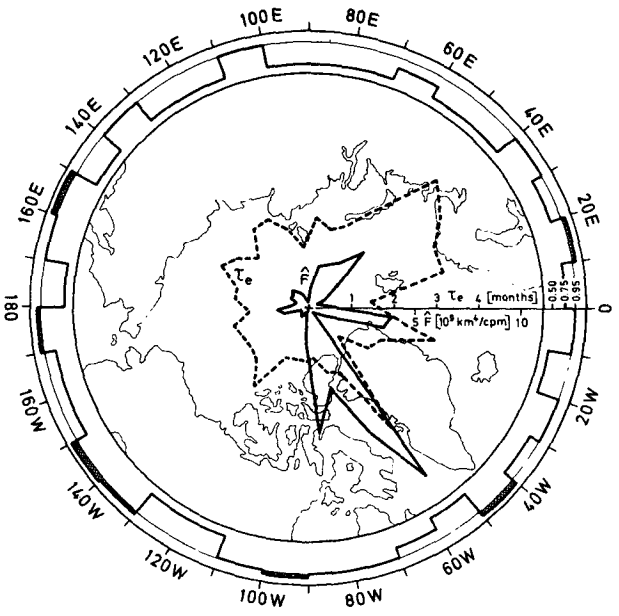

FIG. 20. Longitudinal distribution of white-noise excitation level $\hat{F}$ and relaxation time τ_e in the Arctic.

squares fit of the spectra, the quadratic error expression being normalized in accordance with the maximum likelihood method, by dividing by the variance of the spectral estimates. (See Appendix; Müller *et al.*, 1978; Hasselmann, 1979.) Only periods larger than 4 weeks were used in the fitting procedure to satisfy the requirement of a time scale separation between the response and forcing function appropriate for a Markov process of the form (4) or (5).

The longitudinal dependence of the fitted relaxation time $\tau_e = 1/\lambda$ and the white-noise excitation level $\hat{F}$ is shown in Figs. 20 and 21. The zonal distribution of the excitation level $\hat{F}$ for both the Arctic and Antarctic sea ice is very similar to the distributions for the annual signal and the anomaly variance, Figs. 2 and 5, whereas the zonal distribution of the relaxation time τ_e shows no clear correlation with the magnitude of the forcing or the anomaly.

In the Arctic (Fig. 20), the feedback factor, $\lambda = 1/\tau_e$, is seen to be large in the Siberian and Canadian sectors. This may be attributed to land locking by the Eurasian and American continents, which supports persistence during wintertime, and also to river run off, which tends to stabilize the upper layers of the Arctic Ocean, thereby decreasing the thermal inertia and the relaxation time. The largest relaxation times in the Arctic, of the order of 3–4 months, are found in the Davis Strait, the East Greenland Current and the Barents Sea, in areas in which the interaction between sea ice, ocean and atmosphere is not disturbed by continental influences. In the Antarctic (Fig. 21) the relaxation times (1–2 months) are generally smaller than in the Arctic Basin. This may presumably be attributed to an enhanced ice-ocean interaction in the Southern Ocean (upwelling, divergent Ekman drift, strong ocean currents), and the fact that nearly all Antarctic sea ice is annual ice of 1–2 m thickness, whereas

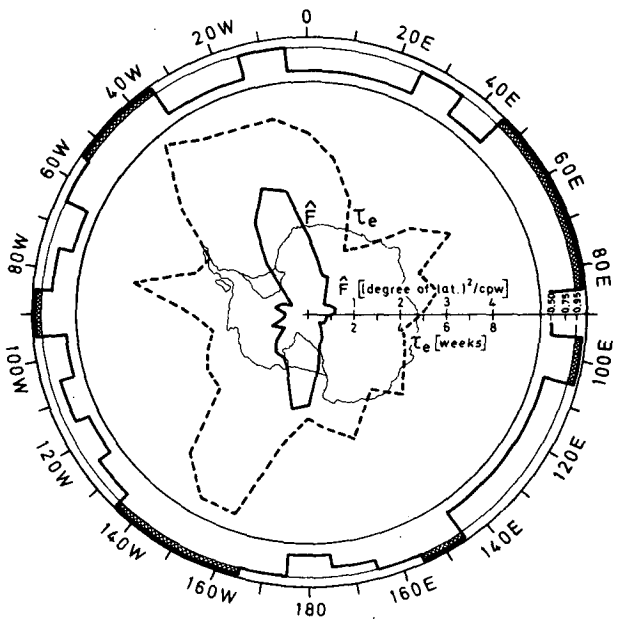

FIG. 21. Longitudinal distribution of white-noise excitation level $\hat{F}$ and relaxation time τ_e in the Antarctic.

80% of the Arctic sea ice is in thicker layers older than two years, and 60% older than 5 years.

The step-function curves shown at the outer margins of Figs. 20 and 21 denote the statistical significance levels at which the optimal fit was acceptable, cross hatching indicating areas for which the Markov model is not acceptable at a 95% significance level (see Appendix). For 7 longitudes in the Arctic and 12 in the Antarctic, the model has to be rejected at this confidence level. It will be shown later that improved fits could generally be achieved by including the interaction of neighboring sectors in the model (advection and diffusion).

The influence of the trend on the analysis of the auto- and cross-spectra was found to be small. Subtraction of the trend slightly reduces the energy at small frequencies and results in an increase in λ (reduction of τ_e), typically of the order of 20% in areas of pronounced trend, but up to a factor of 2 at two longitudes in the Southern Ocean (150°W, 160°W). The white-noise forcing $\hat{F}$ is not affected.

c. *Cross-correlation of Arctic and Antarctic sea ice*

From the common period of the Arctic and Antarctic data sets (January 1973–December 1976) the cross-correlation of the total sea ice cover at both poles was calculated, after removal of the annual cycles computed for the four-year period (the Antarctic data was smoothed to monthly means). The correlation is generally insignificant. A barely significant positive correlation peak of 0.40 is found for $\tau \approx 15$ months (Arctic leading Antarctic) and a similar negative peak (-0.49) at $\tau \approx -25$ months, but one or two peaks of this magnitude are to be expected in the set of all lags. We conclude that in the rather limited period of overlap of the data no significant Arctic-Antarctic correlations were found.

5. Atmospheric forcing

A preliminary inspection of the correlation between ice-anomaly fields and atmospheric anomaly patterns in the Arctic failed to reveal a clear feedback of the ice-anomaly field onto the atmospheric circulation (suitable atmospheric data was not available for the Antarctic). However, a forcing of the ice-anomaly field by atmospheric anomalies could be clearly discerned in the principal Arctic ice-anomaly sectors. Fig. 22 shows, for example, the cross correlation between the sea ice anomalies and the 500–1000 mb thickness anomalies in the Davis Strait (55°W). The thickness anomaly field represents the average along the longitude (55°W) from 50–90° latitude. The pronounced asymmetry of the correlation function indicates a forcing of the ice anomaly by the atmosphere, without significant feedback in the reverse direction. Also shown is the theoretical curve corresponding to the Markov model (5) with a short time-scale atmospheric forcing function, (cf., Frankignoul and Hasselmann, 1977):

$$\hat{R}(k) = \begin{cases} -\sqrt{A/2}\,\dfrac{e^{-(k+1)\nu T}}{\nu^2 T^2}, & k = 1, 2, \ldots \\ -\sqrt{A/2}, & k = 0 \\ -\sqrt{2A}e^{k\lambda T}, & k = -1, -2, \ldots \end{cases} \tag{7}$$

where $A = \lambda\nu T^2/(\nu T - 1)$ and T is averaging time of the data (1 month). The inverse relaxation times of the sea ice (λ) and of the atmospheric forcing (ν) are taken to be $(3.4 \text{ months})^{-1}$ and $(5 \text{ days})^{-1}$, respectively. Computation of the spectra of the 500–1000 mb thickness showed that these are indeed white for periods larger than a month, as required for the model. [The terminology "atmospheric forcing by the 500–1000 mb thickness" should be interpreted here, as in the similar ocean-atmospheric interaction

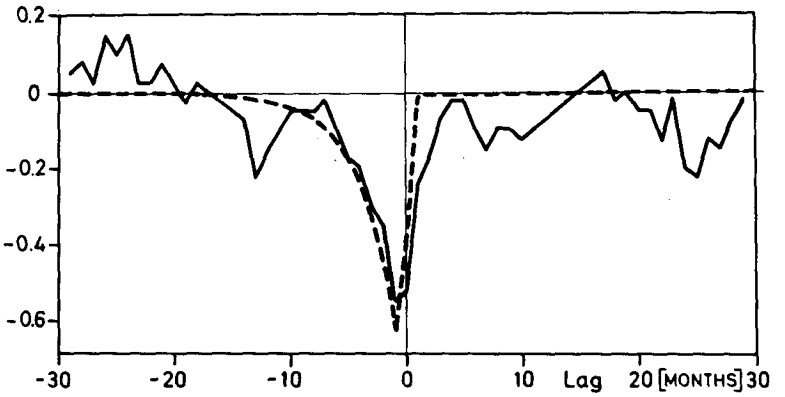

FIG. 22. Cross-correlation function $\hat{R}$ for the sea ice and the 500–1000 mb thickness in the Davis Strait (55°W) (solid line), together with the theoretical curve (dashed line) for a first-order Markov model [Eq. (5)].

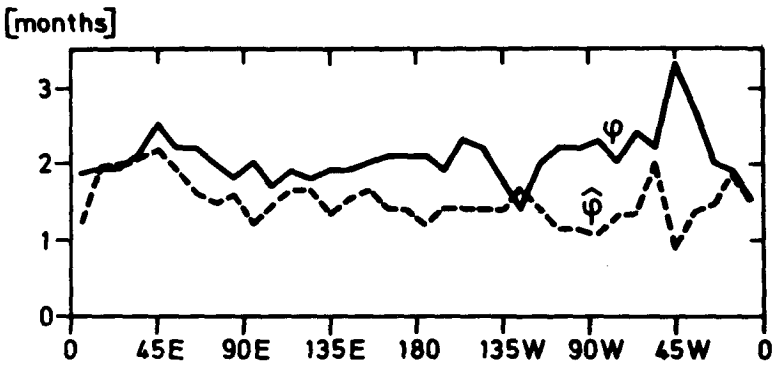

FIG. 23. Longitudinal distribution of the phase φ with which the maximum Arctic sea ice lags behind the minimum solar radiation and the theoretical phase $\hat{\varphi}$ for purely solar input computed from the relaxation times in Fig. 20.

analyses in Davis (1976) and Frankignoul and Hasselmann (1977) in the formal sense, as representative of the true atmospheric forcing, the assumption being that the true forcing function for ice anomalies is significantly correlated with the chosen atmospheric variable.]

6. Seasonal forcing

The thermal inertia of the sea ice response to atmospheric forcing inferred from the white-noise forcing model may be compared with the observed response of the sea ice to seasonal forcing. If the hypothesis is made that sea ice responds directly to the solar radiation and any phase lag between the annual cycle of the sea ice extent and the solar radiation (apparent, for example, in Figs. 1 and 3) is due solely to the inertia of the sea ice system (expressed by the empirical feedback parameter λ) one obtains for the theoretical phase lag $\hat{\varphi}$ of the sea ice cycle relative to the first harmonic of the annual solar radiation

$$\hat{\varphi} = \arctan(\omega_a/\lambda), \tag{8}$$

where ω_a is the annual frequency in radians. The theoretical dependence of $\hat{\varphi}$ on longitude resulting from the empirically determined longitudinal dependence of λ is shown as a dashed line in Figs. 23 and 24. The observed phases (solid lines) are generally higher, the difference between the observed and theoretical phases being larger in the Antarctic than in the Arctic. A plausible explanation for the difference between the theoretical-empirical and observed phases is that the sea ice does not in fact respond directly to the solar radiation alone, but also to the ocean (both directly and via the ocean-atmosphere-sea ice interaction loop). The inertia of the ocean introduces an additional buffer to the system. For linear coupling to the ocean alone, the phases of the oceanic response to the annual solar radiation cycle and the subsequent sea ice response to the ocean simply add.

For the Antarctic the difference between the observed and theoretical-empirical phases of the order of 2 months implies a relaxation time for the ocean alone, assuming no direct coupling of the sea ice to solar radiation, of the order of 3.5 months. This

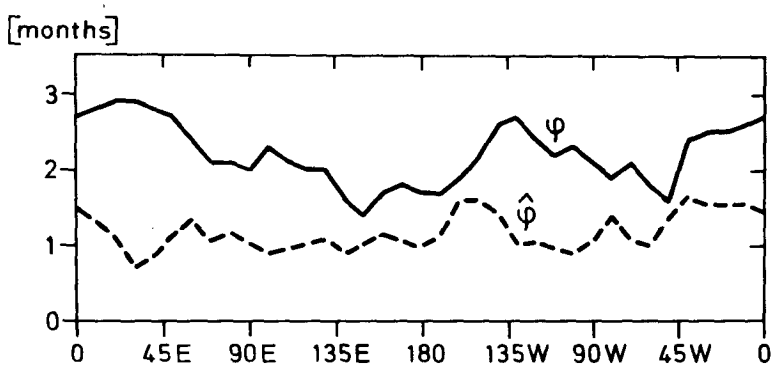

FIG. 24. Longitudinal distribution of the phase φ with which the maximum Antarctic sea ice lags behind the minimum solar radiation and the theoretical phase $\hat{\varphi}$ for purely solar input computed from the relaxation times in Fig. 21.

represents a reasonable response time for the upper ocean (cf., Reynolds, 1978). For the Arctic, however, the corresponding response time varies from essentially 0 up to about 1 month, except for the Greenland sector (45°W), which appears to be dominated by oceanic interactions similar to the Antarctic. From the rather small values of the average Arctic phase differences, it can be estimated that perhaps only half of the seasonal sea ice variation in the Arctic is due to interaction with the ocean, the remaining half resulting from direct solar radiation. This is supported by the observations of Ackley (1979a), who points out that meltwater ponds typical of the Arctic are not found on Weddell sea ice. Thus in contrast to the Arctic Ocean there is little positive albedo feedback, the high albedo of the sea ice in the Antarctic preventing significant absorption of solar energy and ice formation and ablation is mainly determined by oceanic heat fluxes.

The continuous increase of the observed phase shift from the western to the eastern edge of the Weddell Sea (50°W–30°E) is consistent with observations by Ackley (1979a), who interprets this as an eastward advection of the ice edge. The same west-east increase of the observed phase is found in the Ross Sea (180–140°W). Other interpretations of a west-east increase in phase, apart from the straightforward advection, are conceivable. Thus an increase in the thermal inertia of the coupled sea ice-ocean system produces the same effect. However, the phase shift associated with the relaxation time of the sea ice itself, as inferred from the simple uncoupled first-order Markov model (Fig. 24, dashed line), is insufficient to explain the observed increase. An increase in thermal inertia of the ocean of the derived magnitude is consistent with available Weddell Sea data (Carmack and Foster, 1977; Foster and Carmack, 1977). Investigation of the annual sea ice cycle alone is inadequate to decide whether advection (coupled with a required stronger production of sea ice in the western regions of the Weddell and Ross Seas) or a west-east increase of the relaxation time of the ocean is the correct physical interpretation. But the westward advection of sea ice in the Weddell Sea and the Ross Sea inferred from the anomaly cross-spectral analysis (Section 7) suggests the west-east increase of the relaxation time of the ocean as the most probable candidate responsible for the increase in the observed phase shift.

7. A dynamical model

a. A formal Markov model

The simple scalar Markov model (5) yields a satisfactory description of the autospectra (or autocovariance functions) both for the EOF representation (Lemke, 1980) and for most of the individual longitude sectors. The white-noise forcing may be identified, as in previous applications of the stochastic forcing model (Hasselman, 1976; Frankignoul and Hasselmann, 1977; Lemke, 1977; Reynolds, 1978) with the atmospheric forcing associated with short-lived weather disturbances. The stabilizing feedback parameter λ may be attributed to the heat transfer from the ice to either the atmosphere or the ocean or to internal ice-ice interactions; existing parameterizations for these transfer rates all yield a linear stabilizing feedback term for small deviations of the ice-covered area. However, although these models provide some useful numbers on the general magnitude of the forcing and feedback rates, they need to be generalized in order to explain the structure of the nondiagonal elements of the cross-spectra or cross-covariance functions.

In fact, the dependence of the relaxation times of the scalar Markov models for individual EOF amplitudes on the EOF order (Lemke, 1980), i.e., on the scale of the anomaly, already indicates a scale dependence of the relaxation mechanism, as would be expected (e.g., for diffusion or advection processes).

The migration illustrated in Fig. 17 also indicates some form of direct interaction between different sectors.

The effects can be most easily modeled by considering a vector Markov process including nondiagonal terms in the feedback matrix Λ in the form

$$\dot{y}_i(t) = \sum_j \Lambda_{ij} y_j(t) + n_i(t), \quad i = 1, \ldots, 36, \quad (9)$$

where i, j represent the longitudinal indices. In view of the narrow width of the cross-correlation function $R_{i,i+k}(\tau)$ as a function of longitudinal lag k (Figs. 16, 17), we shall limit ourselves to the simplest generalization of (9) in which only the two closest off-diagonal elements are included in the feedback Λ.

The cross-spectral matrix of the vector Markov process (9) is given by

$$\hat{G}_{ij}(\omega) = \sum_{k,l} H_{ik}(\omega) \hat{F}_{kl}(0) H^{+}_{lj}(\omega) \quad (10)$$

where $\mathbf{H} = (i\omega \mathbf{I} - \Lambda)^{-1}$, $\mathbf{I}$ is the unit matrix, $\mathbf{H}^{+}$ is the adjoint (transposed and conjugate complex) matrix of $\mathbf{H}$, and $\hat{\mathbf{F}}$ is the cross-spectrum of the white noise forcing at zero frequency, i.e.

$$\hat{F}_{kl}(0) = \langle n_k(\omega = 0) n_l^*(\omega = 0) \rangle = \int_{-\infty}^{\infty} R_{kl}(\tau) d\tau = \hat{F}_{lk}(0). \quad (11)$$

For a discrete multivariate Markov process

$$y_i(t) = \sum_j \alpha_{ij} y_j(t - \Delta) + n_i(t), \quad (12)$$

the cross spectral matrix is given by (10) with a frequency response matrix $\mathbf{H}$ which is given in this case by

$$\mathbf{H}(\omega) = (\mathbf{I} - \boldsymbol{\alpha} e^{-i\omega\Delta})^{-1}. \quad (13)$$

Since the average diameter of highs or lows in the atmosphere is ~500–1000 km, the cross-spectral matrix $\hat{F}_{ij}$ [Eq. (11)] of the atmospheric forcing is also assumed to consist of only three diagonals ($\hat{F}_{ij} = 0$ for $j > i + 1$ or $j < i - 1$), corresponding to the structure of the feedback matrix $\boldsymbol{\alpha}$. (30 degrees of longitude at 65°N corresponds to a scale of 1400 km.) Because of the time-scale separation the forcing spectrum $\hat{F}_{ij}(\omega)$ is needed only at zero frequency (Hasselmann, 1976); from complex symmetry properties of a spectrum it follows further that $\hat{F}_{ij}(0)$ $[=\hat{F}_{ji}^*(0)] = \hat{F}_{ji}(0)$, since $\hat{F}_{ij}(0)$ is real.

b. A physical model

The model (9) or (12) with a tri-diagonal interaction matrix can be readily interpreted in physical terms. Consider a general transport equation

$$\frac{\partial y}{\partial t} + \mathrm{div} A = S \quad (14)$$

for the sea ice cover y, where A represents the lateral horizontal sea ice flux and S the source or sink of sea ice. The source term S includes freezing and melting of sea ice due to heat exchange with the air above and the ocean below, as well as thickness variations due to divergent or convergent ice flow (ice ridging). The latter appears in S rather than the flux A because it refers to an area measure, not the actual volume. Thus, S is a function of oceanic, ice and atmospheric variables. By averaging over a time period intermediate between the short time scale of atmospheric fluctuations and the longer time scale of sea ice and oceanic variations it can be divided into a mean component $\bar{S}$, depending on ice, ocean and the mean atmospheric conditions, and a fluctuating component S' that describes the influence of short-time weather disturbances,

$$S = \bar{S} + S'. \quad (15)$$

For small excursions about an equilibrium state we assume that $\bar{S}$ can be expanded with respect to the sea ice cover y (linear feedback), so that the transport equation (14) for sea ice anomalies reads

$$\frac{\partial y}{\partial t} + \mathrm{div} A = -\lambda y + n \quad (16)$$

where $n = S'$. In the following we shall assume that λ is constant and will also ignore external slow variations in S caused by the natural variability of the ocean. Thus the interaction with the ocean is modeled only implicitly in the feedback parameter λ, the ocean being treated, in effect, as a time independent heat reservoir. The lateral sea ice flux A is represented as a superposition of an advective and a diffusive flux

$$A = yU - D\frac{\partial y}{\partial x}. \quad (17)$$

The transport equation thus takes the specific form

$$\frac{\partial y(x,t)}{\partial t} = -\lambda(x)y(x,t) + \frac{\partial}{\partial x}\left[D(x)\frac{\partial y(x,t)}{\partial x}\right] - \frac{\partial}{\partial x}[y(x,t)U(x)] + n(x,t), \quad (18)$$

where x denotes the longitude.

Comparing the discretized form of (18) with (12) it is evident that the symmetric part of the next neighbor interaction in (12) is determined by the lateral diffusion coefficient D and the antisymmetric part by the lateral advection U, modified by a term arising from the longitudinal gradient of D

$$\left.\begin{aligned} \alpha_{ii} &= 1 - \lambda_i - 2D_i - \tfrac{1}{2}(U_{i+1} - U_{i-1}) \\ \alpha_{ii+1} &= D_i - \tfrac{1}{2}U_i + \tfrac{1}{4}(D_{i+1} - D_{i-1}) \\ \alpha_{ii-1} &= D_i + \tfrac{1}{2}U_i - \tfrac{1}{4}(D_{i+1} - D_{i-1}) \end{aligned}\right\}. \quad (19)$$

The model contains three feedback parameters for each longitudinal grid point: the local feedback λ, the diffusion coefficient D and the advection coefficient U.

In addition, there are two parameters at each longitudinal grid point that describe the atmospheric forcing, $\hat{F}_{i,i}$ and $\hat{F}_{i,i+1}$.

c. Model class and model hierarchy

The general model [Eq. (12) or Eq. (18)] with different forcing and feedback coefficients for different longitudes is not necessarily the simplest model that describes the data at a given significance level. In order to determine the degree of detail that can be inferred from the data, a hierarchy of models should be tested, starting with a simple model and then introducing more and more coefficients.

A specialized form of (18) or (12) is a rotationally invariant model with longitude independent feedback and forcing matrixes. However, rotationally-symmetric models must be rejected on the basis of the measured cross-spectra of the spatial Fourier components, which are not zero, as required by the model (Lemke, 1980).

A simple generalization of this model is to assume that the statistical correlation between different wavenumbers arises entirely through the statistical correlation of the forcing function. The feedback and next neighbor coupling coefficients are still taken as independent of longitude, but the cross spectrum of the white-noise forcing is now treated as an arbitrary function of longitude. An attempt to fit this model to the observed data was also unsuccessful, basically because the model was unable to reproduce the strong longitudinal variations in the local feed-

back parameter and the structure of the cross-correlation functions shown in Figs. 16, 17, 20 and 21.

Other attempts to simplify the model by introducing rotational invariance constraints on selected variables was also unsuccessful. Thus, all models considered in the following allow full longitudinal freedom of all parameters considered.

An alternative hierarchy of models can be constructed by retaining all longitudinal degrees of freedom but successively introducing the various terms of the interaction matrix. The simplest model considered in this hierarchy assumes that sea ice correlations between different longitudes arise entirely through statistical correlations in the forcing functions: the feedback matrix $\boldsymbol{\alpha}$ in (13) is assumed to contain only diagonal elements, i.e., the local feedback terms without advection and diffusion. In the next higher order model either an advective or a diffusive flux is introduced additionally into A [Eq. (17)]. The highest order model, finally, includes both advective and diffusive fluxes, without restriction of the general form of A. The hierarchy is summarized in the following listing:

Model I:	local feedback λ, no advection or diffusion	(3 parameters per longitudinal gridpoint)
Model IIa:	local feedback λ and advection U	(4 parameters)
Model IIb:	local feedback λ and diffusion D	(4 parameters)
Model III:	local feedback λ, advection U and diffusion D	(5 parameters).

d. Model fitting

The fitting of $\hat{G}$ [Eq. (10)] to observed spectra of the sea ice extent is in general a time consuming numerical operation because at each step of the minimization procedure the feedback matrix $\boldsymbol{\alpha}$ (36 × 36) has to be inverted [cf., Eq. (13)]. This difficulty can be overcome by calculating the cross-spectrum $F_{ij}(\omega)$ of the forcing from Eq. (9):

$$F_{ij}(\omega) = \sum_{k,l} H_{ik}^{-1}(\omega) G_{kl}(\omega) H_{lj}^{-1+}(\omega) \qquad (20)$$

or

$$F_{ij}(\omega) = \sum_{k=i-1}^{i+1} \sum_{l=j-1}^{j+1} (\delta_{ik} - \alpha_{ik} e^{-i\omega\Delta}) \times G_{kl}(\omega)(\delta_{jl} - \alpha_{jl} e^{i\omega\Delta}), \qquad (21)$$

for $j = i - 1, i, i + 1$, where the summations are restricted as indicated because the feedback matrix $\boldsymbol{\alpha}$ consists only of three diagonals. The frequency dependent forcing $\mathbf{F}$ in (21) essentially represents a linear transformation of the data $\mathbf{G}$ and can be regarded as the equivalent measured forcing. This has to be fitted to the model forcing $\hat{\mathbf{F}}$, by suitable adjustment of the model parameters, which is assumed to be constant (white) for all frequencies ω in the climatic frequency range considered (periods larger than 1 month).

An iterative fitting technique was employed, in which the three forcing cross-spectra, $F_{i,i-1}$, F_{ii}, $F_{i,i+1}$, were fitted to the white noise hypothesis at each longitudinal gridpoint, by varying the local forcing and feedback parameters, while all other elements of $\hat{\mathbf{F}}$ and $\boldsymbol{\alpha}$ were held constant. After finding a minimum of the local error function ϵ (see Appendix), the previous parameters for this sector were then replaced by the new parameters, and the next longitudinal gridpoint was treated similarly. The poles were circulated several times until convergence was reached (usually after 4–5 cycles). It should be noted that except for the Model I (with diagonal feedback-matrix $\boldsymbol{\alpha}$) the minimal error solution obtained by this forcing-fit technique is not exactly identical to the solution obtained by minimizing simultaneously the total error function for all sectors.

e. Results

The degrees of success of the model fit are shown as plots of the local error function ϵ (see Appendix) for the four models against longitude in Figs. 25 and 26. As expected, Model I (local feedback only) yields the highest and Model III (local feedback, diffusion and advection) the lowest values of the error function ϵ. At several longitudes, especially in the Arctic, the simple local feedback Model I is acceptable (at a 95% significance level), but in most sectors the highest order model including both symmetric and antisymmetric next neighbor interactions has to be introduced to achieve an acceptable description of the data. In the Arctic, especially in the Atlantic sectors and the East Siberian Sea, Model III yields a distinct improvement compared to Model I. In Antarctica, Model III is clearly better than Model I in the eastern Weddell Sea, East Antarctica, the Ross Sea and the Amundsen Sea, indicating that in these areas the interaction with the next neighbor longitude (lateral diffusion and advection) plays an important role in the overall sea ice dynamics. The poorest description of the data by Model III is achieved in the Southern Ocean in the western Weddell Sea (40–60°W), where the model yields little improvement over the simple Model I (Fig. 26). This is probably due to the particular geography of

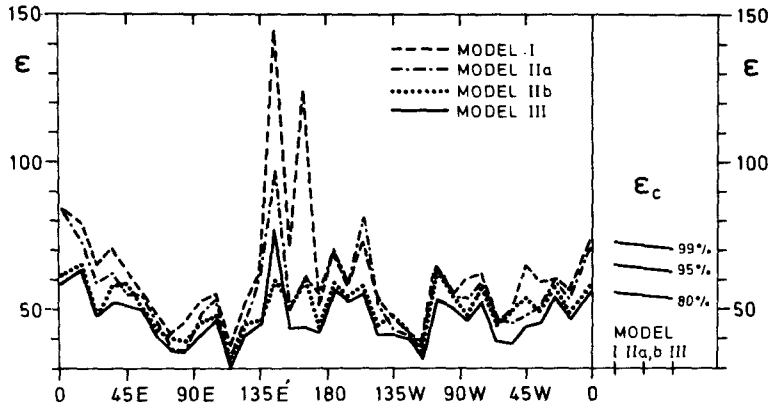

FIG. 25. Longitudinal distribution of the error function ϵ of the Arctic model hierarchy.

the area. The westward movement of the sea ice in the Weddell Sea gyre impinges on the Antarctic Peninsula, where strong ridging occurs, forcing a northward flow (Ackley, 1979b). Our models, including only lateral advection and diffusion, are presumably unable to describe this behavior. The model is also poor in the Bellinghausen Sea (90°W, Fig. 26) and at two longitudes in the South Indian Basin (50°E, 70°E), presumably because lateral interactions are again inadequate to describe the real dynamics in that area.

At both poles, Model IIb (local feedback and lateral diffusion) is in general more realistic than Model IIa (local feedback and lateral advection). This is demonstrated in Fig. 27, showing the total error function $\bar{\epsilon}$ integrated over longitude versus model number. This is especially true for the Arctic sea ice variability, where the diffusion-model (IIb) is significantly better than the advection-model (IIa), but the highest order model (III) provides only a small improvement compared to Model IIb. Thus, lateral advection of sea ice anomalies appears to be of relatively minor importance in the Arctic Ocean. In the Antarctic, however, lateral advection is found to be of comparable importance to lateral diffusion.

The higher levels of the error functions in the Antarctic models compared to the Arctic ones suggest that some characteristics of the Southern Ocean sea ice dynamics, which are not present in the Arctic Ocean, are not covered by the transport equation (16) or (18). A likely candidate is the interaction with the natural variability of the ocean.

Since Model III in the Arctic exceeds $\epsilon_c^{80\%}$ at only four longitudes (which would be expected statistically) the complete model—including non-diagonal atmospheric forcing, local feedback, lateral advection and diffusion in all sectors—is acceptable at the 80% significance level. The Arctic diffusion model (IIb) is similarly acceptable at the less restrictive 95% significance level. Models I and IIa must be rejected.

Except at six sectors in the Bellinghausen Sea (90°W), the South Indian Basin (50°E, 70°E) and the western Weddell Sea (40–60°W), which obviously

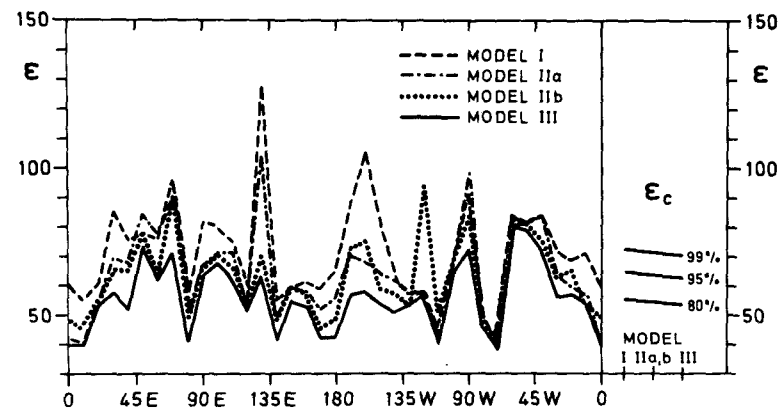

FIG. 26. Longitudinal distribution of the error function ϵ of the Antarctic model hierarchy.

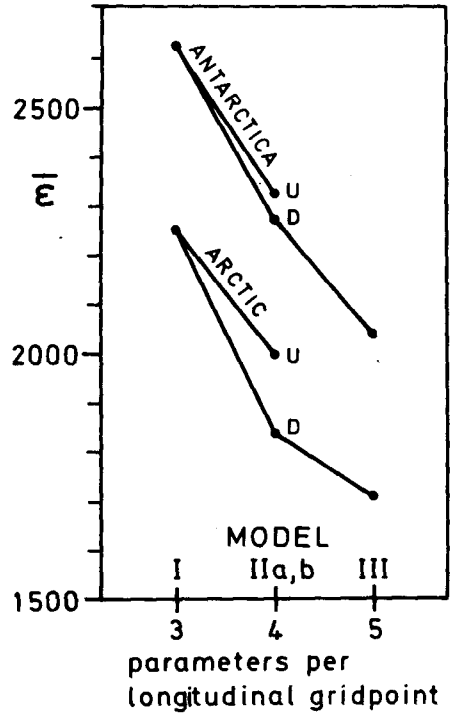

FIG. 27. Error function $\bar{\epsilon}$ integrated over longitude verus model number.

demand additional dynamical parameterizations, Model III is also an acceptable description at the 95% significance level of Antarctic sea ice anomalies.

The longitudinal distribution of the optimal fitted Arctic and Antarctic forcing and feedback parameters inferred from Model III are shown in Figs. 28–34.

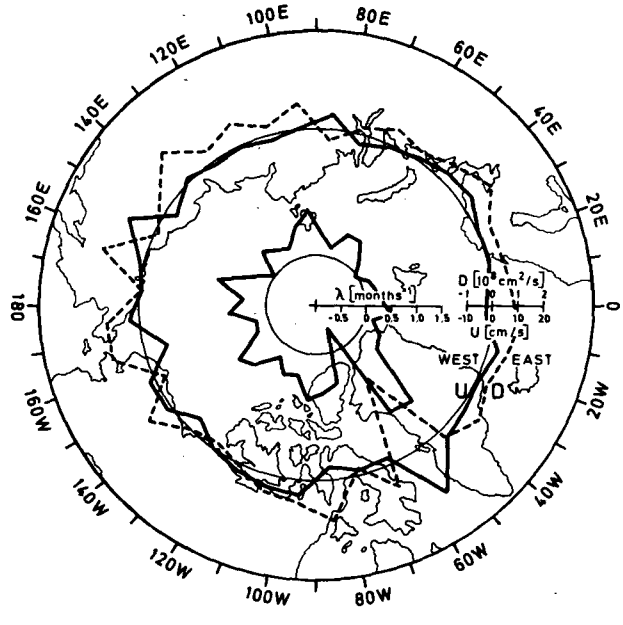

FIG. 28. Longitudinal distribution of lateral diffusion D, advection U and local feedback λ for sea ice anomalies in the Arctic.

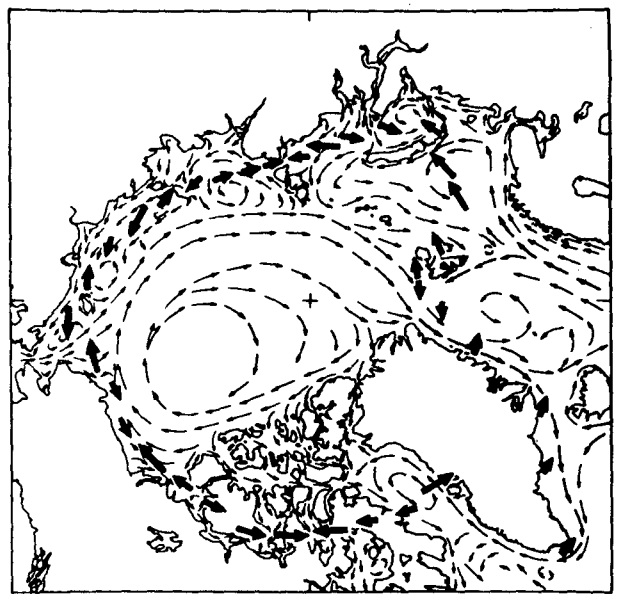

FIG. 29. Arctic Ocean surface circulation (after U.S. Navy Hydrographic Office, 1958) and Arctic sea ice model advection pattern from Fig. 28 (thick arrows).

The diffusion coefficient for the Arctic sea ice (Fig. 28 dashed line) is of the order of 0.5×10^4 m^2 s^{-1}. This is comparable to values often assumed in large scale ocean circulation studies. The values are fairly constant in the Atlantic part of the Arctic, but fluctuate strongly and even become negative in the western Atlantic and East Canadian sectors.

Presumably this implies that the longitudinal sea ice coupling cannot be described simply as a quasi-local (i.e., differential) interaction in these regions. A possible mechanism of longitudinal sea ice coupling, for example, is through atmospheric heat advection. In sectors with large sea ice anomalies, the atmosphere will normally experience increased cooling. The advection of this cold air to neighboring sectors then results in enhanced sea ice formation also in these sectors. If the atmosphere acts in this process only as a relatively short time constant intermediate storage buffer for transporting heat from one sea ice sector to the next, the process can be represented as a combination of local feedback and effective advection (if the wind has a prevailing direction) or diffusion (for variable wind directions). However, if the time-constant for the persistence of atmospheric temperature anomalies is large, or if the effect of ice anomalies on the atmosphere cannot be represented simply as the advection of locally induced temperature changes, but involves, say, a readjustment of the entire atmospheric circulation, the ice-atmosphere-ice interaction loop will extend over many longitudinal sectors and can be simulated only by more complex, non-local operators. Thus, the existence of occasionally negative values of the diffusion coefficient should not necessarily be interpreted as

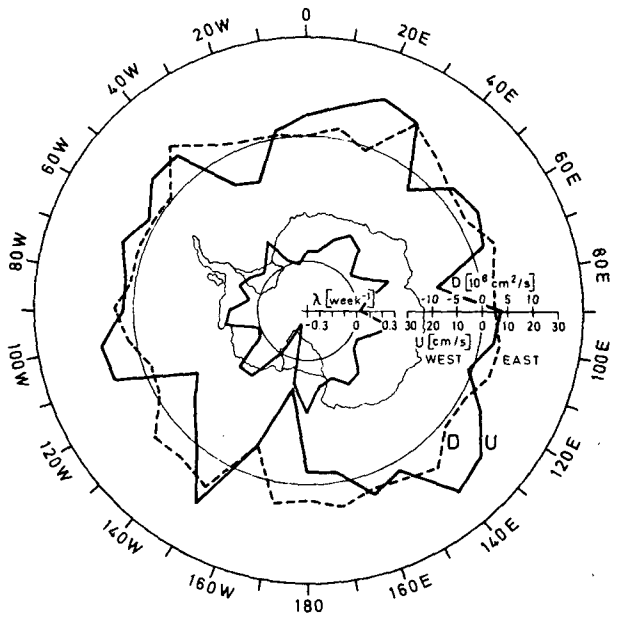

FIG. 30. Longitudinal distribution of lateral diffusion D, advection U and local feedback λ for sea ice anomalies in the Antarctic.

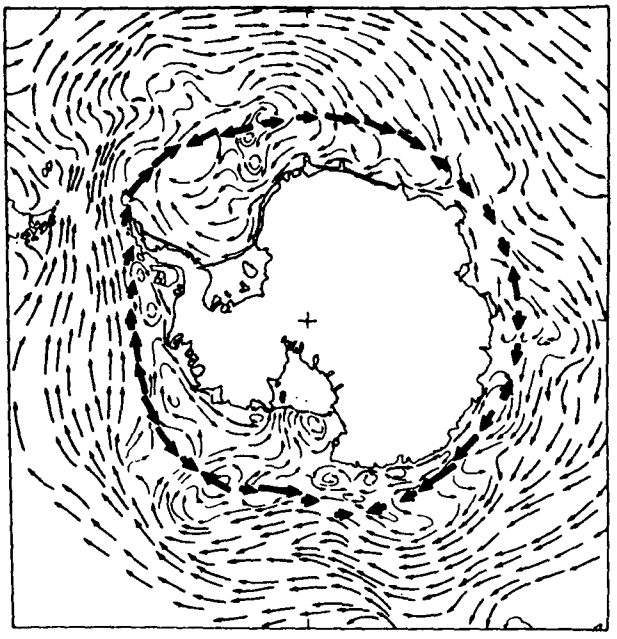

FIG. 31. Southern Ocean surface circulation (after Treshnikov, 1967) and Antarctic sea ice model advection pattern from Fig. 30 (thick arrows).

implying upgradient fluxes, but simply as an attempt to approximate presumably rather complex nonlocal interactions by simple local operators. This applies particularly for the Davis Strait sector in Fig. 28, which has a rather complex geography characterized by a north-south orientation of coasts and sea ice boundaries as opposed to the average east-west orientation of other regions of the Arctic and Antarctic.

The significance of cross-sector interactions is demonstrated by the differences in the local feedback parameters λ_i for the decoupled model (Figs. 20 and 21, where $\tau_e = \lambda^{-1}$) and the complete interactive Model III (Figs. 28 and 30). In the complete models a significant fraction of the net relaxation rate of sea ice anomalies is attributed to advection and diffusion rather than local negative feedback [cf., Eq. (19)].

The advection of sea ice anomalies in the Arctic Ocean (Fig. 28, solid line), especially the eastward flow in the Barents Sea, the East Siberian Sea and the Canadian Archipelago and the westward flow in the Bering Strait are in reasonable qualitative and order of magnitude agreement with the ocean surface circulation patterns near the continental margins, the normal location of sea ice anomalies, according to the ocean surface circulation map of the Arctic of the U.S. Navy Hydrographic Office (1958, see Fig. 29). The mean absolute value of the lateral advection of sea ice anomalies in the Arctic Ocean is of the order of 4 cm s^{-1}.

The advection and diffusion coefficients inferred for the Antarctic are considerably larger than in the Arctic Ocean (Fig. 30). This is as expected because of the greater sea ice-ocean interaction due to upwelling and strong lateral ocean currents in the Antarctic. The mean diffusion coefficient (dashed line, Fig. 30) in the Southern Ocean is of the order of 3×10^4 m^2 s^{-1}, and the mean absolute value of the advection is 11 cm s^{-1}, in rough agreement with typical velocities of ocean surface currents in that area. The advection (solid line, Fig. 30) indicates a

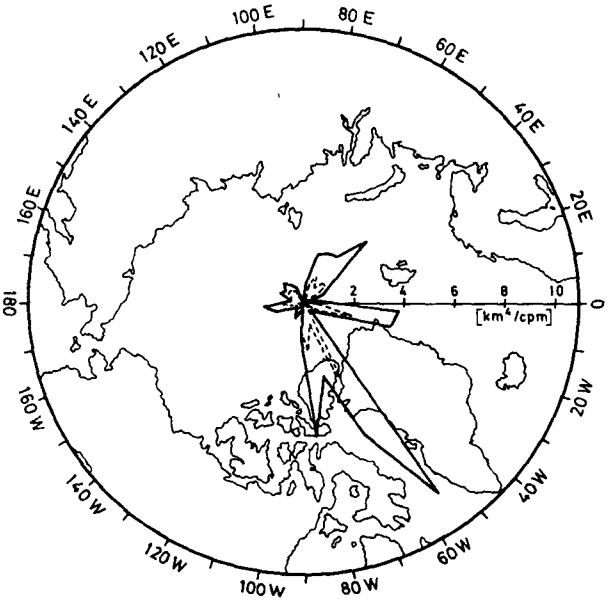

FIG. 32. Longitudinal distribution of the local (solid line) and next neighbor (dashed line) cross-spectral forcing in the Arctic.

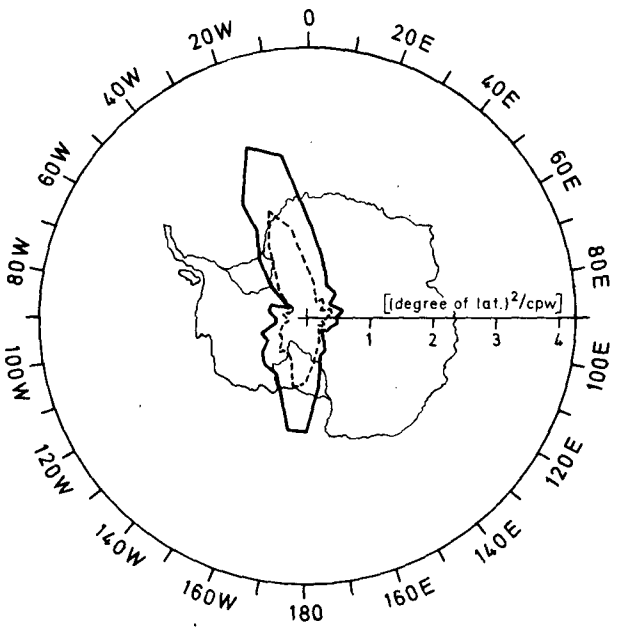

FIG. 33. Longitudinal distribution of the local (solid line) and next neighbor (dashed line) cross-spectral forcing in the Antarctic.

significant westward flow of sea ice anomalies in the Weddell Sea, the Ross Sea and north of the Amery Ice Shelf (80°E) and the Getz Ice Shelf (120°W). In all other parts of the Southern Ocean the sea ice flow is eastward, most strongly east of the Weddell Sea (20°E), in the South Indian Basin (140°E) and in the Amundsen Sea (100°W).

The general flow pattern is in good agreement with the observed ocean surface circulation around Antarctica (Weddell Sea gyre, Ross Sea gyre, Antarctic Circumpolar Current) [Treshnikov, 1967; see Fig. 31].

The longitudinal distribution of the forcing parameters is shown in Figs. 32 and 33. The diagonal elements of the forcing matrix $\hat{\mathbf{F}}$ (solid lines) exhibit the same longitudinal dependence, found previously for the decoupled model, Figs. 20 and 21. Thus, the introduction of lateral interaction between sea ice anomalies does not affect the local forcing. The non-diagonal forcing terms (dashed lines), representing the cross-spectrum of the forcing with the eastern neighbor longitudinal gridpoint, show the same longitudinal dependence as the diagonal elements, but are considerably smaller. This is consistent with the typical correlation scales of atmospheric disturbance patterns.

Fig. 34 finally shows an example of the hypothetical model-auto-spectrum of the forcing $\hat{F}_{10°E,10°E}$ at 10°E in the Southern Ocean and the real and imaginary part of the cross-spectral forcing $\hat{F}_{10°E,20°E}$ together with the measured forcing $F_{10°E,10°E}$ and $F_{10°E,20°E}$ corresponding to the optimally-fitted model. The hypothetical white noise character is seen to be reproduced reasonably well by the fitted model.

8. Conclusions

The statistical space-time structure of sea ice anomalies for the Arctic (1966–76) and Antarctic (1973–79) can be satisfactorily explained by a dynamical model based on white-noise atmospheric

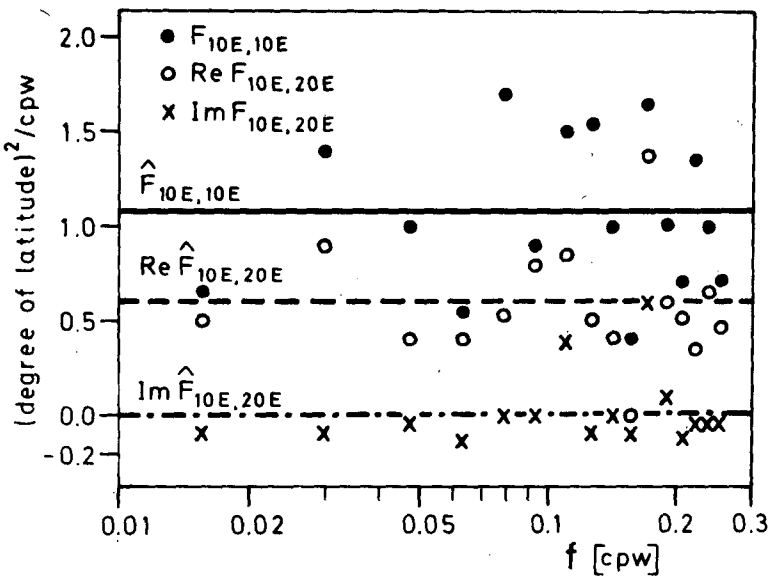

FIG. 34. Comparison of forcing spectra inferred from the best-fit model and the theoretical white-noise forcing spectra at 10°E in the Southern Ocean.

forcing, local stabilizing relaxation and lateral diffusion and advection. Attempts to fit the data with still simpler models were unsuccessful, with the possible exception of the Model IIb without advection for the Arctic. More sophisticated models cannot be distinguished from the present model within the available limited 11-year (6-year) statistics.

Nothing is said about the mechanisms of the local feedback and the lateral coupling between adjacent sea ice anomalies. Thus, the processes could be due to either oceanic or atmospheric interactions. The resolution of this question will require a more detailed joint analysis of both ice-anomaly and atmospheric and sea-surface temperature anomaly fields. Nevertheless, the model presented provides a reasonably consistent physical picture, in general agreement with existing qualitative concepts of sea ice-ocean-atmosphere interactions. It provides a basis for constructing more sophisticated dynamical models or for developing empirical sea ice prediction models for periods up to approximately six months.

An obvious extension of the model which may be expected to improve the dynamical description and extend the range of prediction is the harmonic expansion of the statistics and the model parameters with respect to the annual cycle. Results presented in this paper may be regarded as the zeroth harmonic component of this expansion.

APPENDIX

Multivariate Least-Squares Fit

A statistical test of the validity of models fitted to statistically variable data sets usually consists of three steps.

1. Define an error function ϵ as a suitably weighted measure of the deviations of the optimal fitted model vector $\hat{\mathbf{G}}(a_i)$, depending on the model parameters a_i, from the data vector $\mathbf{G}$.
2. Calculate the probability density function of ϵ under the hypothesis that the model would fit the error-free data perfectly.
3. Choose a critical ϵ_c, defining a particular probability level for $\epsilon < \epsilon_c$ (usually 95%). If the value ϵ of the fitted model exceeds ϵ_c, the model is then rejected at that significance level.

The optimal error function for a multivariate least-squares fit can be shown to be (Linnik, 1961)

$$\epsilon = \sum_{i,j} M_{ij}(G_i - \hat{G}_i)(G_j - \hat{G}_j)^* \qquad \text{(A1)}$$

where $\mathbf{M}$ is the inverse of the covariance matrix $B_{ij} = \langle \delta G_i \delta G_j^* \rangle$ of the data errors δG_i. The deviations $\delta\mathbf{G} = \mathbf{G} - \bar{\mathbf{G}}$ of the data from their true values $\bar{\mathbf{G}}$ induce errors in the fitted model $\hat{\mathbf{G}}(a_i)$, which can be calculated from the least-squares condition $\partial\epsilon/\partial a_i = 0$. In matrix notation one obtains

$$\delta\hat{\mathbf{G}} = \mathbf{T}\delta\mathbf{G}, \qquad \text{(A2)}$$

where

$$\mathbf{T} = \mathbf{C}(\mathbf{C}^+\mathbf{M}\mathbf{C})^{-1}\mathbf{C}^+\mathbf{M}, \qquad \text{(A3)}$$

$$C_{ij} = \partial\hat{G}_i/\partial a_j. \qquad \text{(A4)}$$

Here $\mathbf{C}^+$ denotes the adjoint (transpose and conjugate complex) of $\mathbf{C}$. The error function is accordingly given by

$$\epsilon = (\delta\mathbf{G} - \delta\hat{\mathbf{G}})^+\mathbf{M}(\delta\mathbf{G} - \delta\hat{\mathbf{G}}). \qquad \text{(A5)}$$

If the data errors are Gaussian (for spectral estimates this is approximately the case) the model errors $\delta\hat{\mathbf{G}}$ are also Gaussian, since $\delta\hat{\mathbf{G}}$ is a linear transformation of $\mathbf{G}$. The error function being a quadratic form of Gaussian variables is accordingly approxmately χ^2 distributed.

It can be shown (cf., Linnik, 1961; Lemke, 1980) that the number of degrees of freedom ν of the χ^2 distribution of ϵ is a maximum for the optimal matrix $\mathbf{M} = \mathbf{B}^{-1}$ and is then given by $\nu = p - q$, where p is the number of data and q the number of parameters of the model.

In our application the data consists of auto- and cross-spectral estimates. The general covariance matrix of the finite sampling errors of cross-spectral estimates is given by (Jenkins and Watts, 1968)

$$\langle \delta G_{ij}(\omega)\delta G_{lm}(\omega)\rangle = 2\mu^{-1}\Gamma_{jm}(\omega)\Gamma_{li}(\omega), \qquad \text{(A6)}$$

where Γ is the true cross-spectrum and μ denotes the degrees of freedom of each spectral point. Since we are testing the hypothesis of a true model $\hat{\mathbf{G}}$, Γ is set to equal $\hat{\mathbf{G}}$ in (A6).

REFERENCES

Ackley, S. F., 1979a: Mass balance aspects of Weddell Sea pack ice. *Glaciology*, **24**, 391–405.

——, 1979b: Drifting buoy measurements on Weddell Sea pack ice. *Antarct. J. U.S.* (in press).

Carmack, E. C., and T. D. Foster, 1977: Water masses and circulation in the Weddell Sea. *Polar Oceans*, M. J. Dunbar, Ed., Arctic Institute of North America, Calgary, Canada.

Davis, R. E., 1976: Predictability of sea surface temperature and sea level pressure anomalies over the North Pacific Ocean. *J. Phys. Oceanogr.*, **6**, 249–266.

Foster, T. D., and E. C. Carmack, 1977: Antarctic bottom water formation. *Polar Oceans*, M. J. Dunbar, Ed., Arctic Institute of North America, Calgary, Canada.

Frankignoul, C., and K. Hasselmann, 1977: Stochastic climate models, Part II. Application to sea-surface temperature anomalies and thermocline variability. *Tellus*, **29**, 289–305.

Gordon, A. L., and H. W. Taylor, 1975: Seasonal change of Antarctic sea ice cover. *Science*, **187**, 346–347.

——, ——, and D. T. Georgi, 1977: Antarctic oceanographic zonation. *Polar Oceans*, M. J. Dunbar, Ed., Arctic Institute of North America, Calgary, Canada.

Hasselmann, K., 1976: Stochastic climate models, Part I. Theory. *Tellus*, **28**, 473–485.

——, 1979: Linear statistical models. *Dyn. Atmos. Oceans*, **3**, 501–521.

Hibler, W. D., 1979: A dynamic thermodynamic sea ice model. *J. Phys. Oceanogr.*, **9**, 815–846.

Jenkins, G. M., and D. G. Watts, 1968: *Spectral Analysis and Its Applications*. Holden-Day, 525 pp.

Lemke, P., 1977: Stochastic climate models, Part 3. Application to zonally-averaged energy models. *Tellus*, **29**, 385–392.

——, 1980: Application of the inverse modeling technique to Arctic and Antarctic sea ice anomalies. Ph.D. thesis, Hamburger Geophysikalische Einzelschriften.

Linnik, Yu. V., 1961: *Methods of Least Squares and Principles of the Theory of Observations*. Pergamon, 360 pp.

Lorenz, E. N., 1959: Empirical orthogonal functions and statistical weather prediction. Rep. No. 1, Statistical Forecasting Project, Dept. of Meteorology, MIT.

Müller, P., D. J. Olbers and J. Willebrand, 1978: The IWEX spectrum. *J. Geophys. Res.*, **83**, 479–500.

Parkinson, C. L., and W. M. Washington, 1979: A large-scale numerical model of sea ice. *J. Geophys. Res.*, **84**, 311–337.

Rayner, J. N., and D. A. Howarth, 1979: Antarctic sea ice: 1972–1975. *Geogra. Rev.*, **69**, 202–223.

Reynolds, R. W., 1978: Sea surface temperature anomalies in the North Pacific Ocean. *Tellus*, **30**, 97–103.

Sanderson, R. M., 1975: Changes in the area of Arctic sea ice 1966 to 1974. *Meteor. Mag.*, **104**, 313–323.

Treshnikov, A. F., 1967: Surface water circulation in the Antarctic Ocean. *Soviet Antarctic Expedition*, Vol. 5, 81–83 (English translation).

U.S. Navy Hydrographic Office, 1958: *Oceanographic Atlas of the Polar Seas*, Part II, *Arctic*. Washington, 149 pp.

van Loon, H., and J. C. Rogers, 1978: The seesaw in winter temperatures between Greenland and Northern Europe. Part I: General description. *Mon. Wea. Rev.*, **106**, 296–310.

Walsh, J. E., and C. M. Johnson, 1979a: An analysis of Arctic sea ice fluctuations, 1953–77. *J. Phys. Oceanogr.*, **9**, 580–591.

——, and ——, 1979b: Interannual atmospheric variability and associated fluctuations in Arctic sea ice extent. *J. Geophys. Res.*, **84**, 6915–6928.